

Supporting Information

Rossi et al. 10.1073/pnas.1708064114

1. Low Reynolds Number Swimming with Periodic Beats: Derivation of the Evolution Equations

We show here how to derive Eqs. 1 and 2 of the main text, starting from basic laws of low Reynolds number physics. The motion of a swimmer is determined by a map Φ_t defined on a set \mathcal{B} , the reference body, with values in \mathcal{B}_t , the body of the swimmer at time t . We can write

$$\Phi_t = \mathbf{c}(t) + \mathbf{R}(t)\bar{\Phi}_t, \quad [\text{S1}]$$

where $\mathbf{c}(t)$ is the center of a reference frame moving with the body and $\mathbf{R}(t)$ determines the rotation of the moving frame. The map $\bar{\Phi}_t$ defines the shape of the swimmer at every t , assumed to be periodic with period T_b .

Given a periodic $\bar{\Phi}_t$, the time evolution of $\mathbf{c}(t)$ and $\mathbf{R}(t)$ are determined by the swimmer–fluid hydrodynamic interaction. The total force \mathbf{f} and the total moment \mathbf{g} (with respect to \mathbf{c}) exerted by the fluid on the swimmer are

$$\mathbf{f} = \int_{\partial\mathcal{B}_t} \mathbf{S}\boldsymbol{\nu} dA \quad \text{and} \quad \mathbf{g} = \int_{\partial\mathcal{B}_t} (\mathbf{x} - \mathbf{c}) \times \mathbf{S}\boldsymbol{\nu} dA, \quad [\text{S2}]$$

where \mathbf{S} is the stress tensor in the fluid and $\boldsymbol{\nu}$ denotes the outer unit normal to the boundary $\partial\mathcal{B}_t$ of the swimmer's body \mathcal{B}_t . By neglecting the swimmer's inertia, the equations of motion for the swimmer are given by

$$\mathbf{f} = \mathbf{0} \quad \text{and} \quad \mathbf{g} = \mathbf{0}. \quad [\text{S3}]$$

The stress tensor \mathbf{S} is determined by the (Eulerian) velocity field of the fluid $\mathbf{u}(\mathbf{x}, t)$ at $\partial\mathcal{B}_t$, and the associated pressure. We write $\mathbf{S}[\mathbf{u}]$ to denote the stress tensor associated with the field \mathbf{u} . From the no-slip boundary condition $\mathbf{u} = d\Phi_t/dt \circ \bar{\Phi}_t^{-1}$ and Eq. S1 we have

$$\mathbf{u}(\mathbf{x}, t) = \mathbf{v} + \boldsymbol{\omega} \times (\mathbf{x} - \mathbf{c}) + \mathbf{R} \frac{d\bar{\Phi}_t}{dt} \circ \bar{\Phi}_t^{-1} \left(\mathbf{R}^T (\mathbf{x} - \mathbf{c}) \right) \quad [\text{S4}]$$

for every point \mathbf{x} in $\partial\mathcal{B}_t$, where \mathbf{v} and $\boldsymbol{\omega}$ are the translational and angular velocity of the moving reference frame, respectively. For low Reynolds number flows, the stress tensor is linear with respect to the boundary velocity argument \mathbf{u} . We suppose that the resulting stress tensor has the following property (homogeneity and isotropy):

$$\mathbf{S}[\mathbf{u}] \circ \mathcal{R} = \mathbf{R}\mathbf{S} \left[\mathbf{R}^T \mathbf{u} \circ \mathcal{R} \right] \mathbf{R}^T, \quad [\text{S5}]$$

where we have denoted by \mathcal{R} the rigid transformation $\mathcal{R}\mathbf{x} = \mathbf{c} + \mathbf{R}\mathbf{x}$. Property S5 is satisfied, for example, in the case of a single swimmer moving in a homogeneous and isotropic fluid occupying the whole 3D ambient space, and at rest at infinity. By making the hypothesis that Eq. S5 holds also in our concrete experimental setup, we are assuming that the effects of walls and physical boundaries, of the presence of other swimmers, and so on, are, in fact, negligible.

Plugging the expression in Eq. S4 into $\mathbf{S}[\mathbf{u}]$ and then in Eq. S2, using the property in Eq. S5 together with the linearity of the stress tensor, we can rewrite (after some calculations) Eq. S3 in the following way:

$$\begin{pmatrix} \bar{\mathbf{v}} \\ \bar{\boldsymbol{\omega}} \end{pmatrix} = - \begin{pmatrix} \bar{\mathbf{A}} & \bar{\mathbf{B}} \\ \bar{\mathbf{B}}^T & \bar{\mathbf{C}} \end{pmatrix}^{-1} \begin{pmatrix} \bar{\mathbf{f}} \\ \bar{\mathbf{g}} \end{pmatrix}, \quad [\text{S6}]$$

where we have defined the translational $\bar{\mathbf{v}} = \mathbf{R}^T \mathbf{v}$ and angular $\bar{\boldsymbol{\omega}} = \mathbf{R}^T \boldsymbol{\omega}$ velocities as seen from the reference frame moving with the body. The t -dependent matrix in Eq. S6 is (the inverse of) the “grand resistance matrix” (31) of the swimmer: It quantifies the viscous resistance to rigid motion of the swimmer at its current shape $\bar{\Phi}_t$. The vectors $\bar{\mathbf{f}}$ and $\bar{\mathbf{g}}$ are the force and moment that would act on the swimmer if it was held fixed at one point (and orientation), as a consequence of its shape change. All of the quantities in the right-hand side of Eq. S6 depend only on $\bar{\Phi}_t$ and its time derivative. Hence, they are all T_b -periodic, which implies the periodicity of $\bar{\mathbf{v}}$ and $\bar{\boldsymbol{\omega}}$. From the definitions of $\bar{\mathbf{v}}$ and $\bar{\boldsymbol{\omega}}$ we have that

$$\frac{d\bar{\mathbf{c}}}{dt}(t) = \mathbf{R}(t)\bar{\mathbf{v}}(t) \quad \text{and} \quad \frac{d\bar{\mathbf{R}}}{dt}(t) = \mathbf{R}(t)[\bar{\boldsymbol{\omega}}(t)]_{\times}, \quad [\text{S7}]$$

where $[\bar{\boldsymbol{\omega}}]_{\times}$ is the axial tensor of $\bar{\boldsymbol{\omega}}$ (defined as the skew-symmetric tensor such that $[\bar{\boldsymbol{\omega}}]_{\times} \mathbf{a} = \bar{\boldsymbol{\omega}} \times \mathbf{a}$ for every vector \mathbf{a}). Then, the evolution of the reference frame of a periodically beating swimmer must be the general solution of Eq. S7, where $\bar{\mathbf{v}}$ and $\bar{\boldsymbol{\omega}}$ are taken to be generic T_b -periodic vectors. In the remainder of this section we show that the integration of Eq. S7 leads to Eqs. 1 and 2.

From the second equation in Eq. S7, since $[\bar{\boldsymbol{\omega}}]_{\times}$ is T_b -periodic and skew-symmetric, we have that

$$\frac{d}{dt} \left(\mathbf{R}(t + T_b) \mathbf{R}(t)^T \right) = \mathbf{0}.$$

Thus, $\mathbf{R}(t + T_b) \mathbf{R}(t)^T$ is a t -independent rotation. We denote by \mathbf{n} the unit vector determining the rotation axis of $\mathbf{R}(t + T_b) \mathbf{R}(t)^T$, and by $\Delta\psi$ the rotation angle. Using the same notations we have adopted in the main text we write

$$\mathbf{R}_n(\Delta\psi) = \mathbf{R}(t + T_b) \mathbf{R}(t)^T, \quad \text{for every } t \geq 0. \quad [\text{S8}]$$

Clearly, if $\mathbf{R}(t + T_b) \mathbf{R}(t)^T$ is the identity matrix we do not have a unique choice for \mathbf{n} . This is not the case for the rotatory motion of the *Euglena* studied here, so in the following we will assume that \mathbf{n} is defined unambiguously and $\Delta\psi \neq 0$.

From Eq. S8 it follows that $\mathbf{R}(t + kT_b) = \mathbf{R}_n(k\Delta\psi) \mathbf{R}(t)$ for every integer $k \geq 0$. Therefore, if we consider

$$\tilde{\mathbf{R}}_b(t) := \mathbf{R}_n(\Delta\psi t/T_b)^T \mathbf{R}(t), \quad [\text{S9}]$$

we have (after a simple check) that $t \mapsto \tilde{\mathbf{R}}_b(t)$ describes a T_b -periodic rotation. Eq. 2 follows then from Eq. S9 by taking $\omega = \Delta\psi/T_b$. From the first equation in Eq. S7 and the periodicity of $\tilde{\mathbf{v}}$, and from Eq. S8, we have that

$$\frac{d}{dt}(\mathbf{c}(t + T_b) - \mathbf{R}_n(\Delta\psi)\mathbf{c}(t)) = \mathbf{0}.$$

Then, there exists a t -independent vector \mathbf{d} such that

$$\mathbf{d} = \mathbf{c}(t + T_b) - \mathbf{R}_n(\Delta\psi)\mathbf{c}(t). \quad [\text{S10}]$$

From Eq. S10, in particular, it follows that

$$\mathbf{c}(t + kT_b) = \begin{cases} \mathbf{c}(t) & \text{for } k = 0, \\ \mathbf{d} + \mathbf{R}_n(\Delta\psi)\mathbf{c}(t) & \text{for } k = 1, \\ \sum_{j=0}^{k-1} \mathbf{R}_n(j\Delta\psi)\mathbf{d} + \mathbf{R}_n(k\Delta\psi)\mathbf{c}(t) & \text{for every integer } k > 1. \end{cases} \quad [\text{S11}]$$

If we define $\mathbf{d}_{//} := (\mathbf{d} \cdot \mathbf{n})\mathbf{n}$ and $\mathbf{d}_{\perp} := \mathbf{d} - \mathbf{d}_{//}$, after some algebra we can rewrite Eq. S11 in closed form as

$$\mathbf{c}(t + kT_b) = \underbrace{\mathbf{R}_n(k\Delta\psi)\mathbf{r}_{\perp} + \mathbf{d}_{//}k - \mathbf{r}_{\perp}}_{H_k} + \mathbf{R}_n(k\Delta\psi)\mathbf{c}(t) \quad [\text{S12}]$$

for every integer $k \geq 0$, with $\mathbf{r}_{\perp} := -(\mathbf{d}_{\perp} + \cot(\Delta\psi/2)\mathbf{n} \times \mathbf{d}_{\perp})/2$ (notice that \mathbf{r}_{\perp} is orthogonal to \mathbf{n}). Consider the expression H_k underlined by the curly brace in the right-hand side of Eq. S12. For every integer k , it gives a point that lies on a helix of axis parallel to \mathbf{n} passing through the origin \mathbf{o} . We can parametrize such a helix with the t -dependent curve

$$\mathbf{c}_h^0(t) := \mathbf{R}_n(\Delta\psi t/T_b)\mathbf{r}_{\perp} + \mathbf{d}_{//}t/T_b - \mathbf{r}_{\perp}.$$

A simple check shows that the curve $\tilde{\mathbf{c}}_b^0$ defined as

$$\tilde{\mathbf{c}}_b^0(t) := \mathbf{R}_n(\Delta\psi t/T_b)^T(\mathbf{c}(t) - \mathbf{c}_h^0(t))$$

is T_b -periodic. Thus, the general solution for $\mathbf{c}(t)$ of Eq. S7 can be written as the sum of a helix $\mathbf{c}_h^0(t)$ and a term $\mathbf{R}_n(\Delta\psi t/T_b)\tilde{\mathbf{c}}_b^0(t)$ where $\tilde{\mathbf{c}}_b^0$ is a T_b -periodic “swirl,” as we called it in the main text. Eq. 1 then follows. We remark that there is not a unique choice for the helix and the swirl. Indeed, fix any constant vector \mathbf{r} and take $\mathbf{c}_h(t) := \mathbf{c}_h^0(t) + \mathbf{R}_n(\Delta\psi t/T_b)\mathbf{r}$ and $\tilde{\mathbf{c}}_b(t) := \tilde{\mathbf{c}}_b^0(t) - \mathbf{r}$. Clearly \mathbf{c}_h is still a circular helix (same pitch, different radius) while $\tilde{\mathbf{c}}_b(t)$ is a T_b -periodic curve, and we have again Eq. 1. However, when one helix is fixed, then the swirl is uniquely determined, and vice versa.

2. Cell Body Motion Reconstruction: Parametrization of the Moving Reference Frame and Data Fitting

In this section we give the detailed parametrization of the *Euglena*'s moving reference frame. We also provide more details on the data-fitting procedure (discussed in broad terms in the main text) used to reconstruct the 3D cell body kinematics from 2D microscopy images.

First, some definitions. We fix the laboratory frame as in Fig. S1: The \mathbf{y} and \mathbf{z} axes, as well as the origin $\mathbf{o} = (0, 0, 0)$ of the laboratory frame, lie on the focal plane, while the \mathbf{x} axis is directed toward the observer. The reference frame of the *Euglena* is determined by the time-dependent unit vectors $\mathbf{i}(t)$, $\mathbf{j}(t)$, and $\mathbf{k}(t)$. The vector $\mathbf{k}(t)$ is aligned with the major axis of the ellipsoidal body of the *Euglena*, and it is directed toward the flagellum. The vector $\mathbf{i}(t)$ is defined so that the eyespot point $\mathbf{e}(t)$ lies on the plane generated by $\mathbf{i}(t)$ and $\mathbf{k}(t)$. That is, there are two (positive) constants e_i and e_k such that

$$\mathbf{e}(t) = \mathbf{i}(t)e_i + \mathbf{k}(t)e_k + \mathbf{c}(t). \quad [\text{S13}]$$

The center \mathbf{c} of the reference frame, as stated in the main text, is located at the geometric center of the ellipsoidal body of the cell.

To parameterize the helical trajectory of the center \mathbf{c} we introduce a “helix reference frame” with origin \mathbf{o}_h and orientation determined by three orthogonal unit vectors \mathbf{l} , \mathbf{m} , and \mathbf{n} (Fig. S1). The vector \mathbf{n} defines the helix axis. We suppose that \mathbf{o}_h , \mathbf{n} , and \mathbf{m} lie on the focal plane (a hypothesis which is a posteriori justified by the good agreement between our model and the experimental data), thus $\mathbf{o}_h = (0, o_y, o_z)$. The vector \mathbf{l} is aligned with the \mathbf{x} axis. The angle θ_n , formed by \mathbf{n} and the horizontal, determines the orientation of the frame completely.

We can write the general solution for \mathbf{c} in terms of cylindrical coordinates with respect to the helix reference frame as follows:

$$\begin{aligned} \mathbf{c}(t) &= \mathbf{o}_h + \rho(t)(\mathbf{l}\cos\psi(t) + \mathbf{m}\sin\psi(t)) + \mathbf{n}\zeta(t) \quad \text{with} \\ \rho(t) &= \tilde{\rho}_b(t), \quad \psi(t) = \Delta\psi t/T_b + \tilde{\psi}_b(t), \quad \text{and} \quad \zeta(t) = \Delta\zeta t/T_b + \tilde{\zeta}_b(t), \end{aligned} \quad [\text{S14}]$$

where $\Delta\psi$ and $\Delta\zeta$ are constants, while $\tilde{\rho}_b$, $\tilde{\psi}_b$, and $\tilde{\zeta}_b$ are T_b -periodic functions. The center \mathbf{c} of the body lies in the plane spanned by \mathbf{l} and \mathbf{m} at time $t = 0$, so that

$$\zeta(0) = 0. \quad [\text{S15}]$$

We parametrize the general solution for the rotation $\mathbf{R}(t) = (\mathbf{i}(t)|\mathbf{j}(t)|\mathbf{k}(t))$ of the body frame as

$$\begin{aligned} \mathbf{R}(t) &= \mathbf{R}_n(\alpha(t))\mathbf{R}_m(\beta(t))\mathbf{R}_n(\gamma(t))\mathbf{U}(\theta_n) \quad \text{with} \\ \alpha(t) &= \Delta\psi t/T_b + \tilde{\alpha}_b(t), \quad \beta(t) = \tilde{\beta}_b(t), \quad \text{and} \quad \gamma(t) = \tilde{\gamma}_b(t), \end{aligned} \quad [\text{S16}]$$

where $\mathbf{U}(\theta_n) = \mathbf{R}_l(\theta_n - \pi/2)$, while $\tilde{\alpha}_b$, $\tilde{\beta}_b$, and $\tilde{\gamma}_b$ are T_b -periodic functions.

In the remainder of this section we show how to determine the following list of parameters

$$\xi = \{T_b, \mathbf{o}_h, \theta_n, \Delta\psi, \Delta\zeta, \mathcal{F}\} \cup \{e_i, e_k\} \quad [\text{S17}]$$

which describes completely the cell-body kinematics. The coefficients e_i and e_k , defined in Eq. S13, are auxiliary parameters needed to determine the other ones which, in turn, determine the time evolution of \mathbf{c} and \mathbf{R} . In Eq. S17 we have denoted by \mathcal{F} the set of Fourier coefficients of the T_b -periodic functions defined in Eqs. S14 and S16. We consider only Fourier coefficients up to order one, thus

$$\begin{aligned}\tilde{\rho}_b(t) &= a_\rho + b_\rho \cos(2\pi t/T_b - \phi_\rho), & \tilde{\psi}_b(t) &= a_\psi + b_\psi \cos(2\pi t/T_b - \phi_\psi) \\ \tilde{\zeta}_b(t) &= a_\zeta + b_\zeta \cos(2\pi t/T_b - \phi_\zeta), & \tilde{\alpha}_b(t) &= a_\alpha + b_\alpha \cos(2\pi t/T_b - \phi_\alpha) \\ \tilde{\beta}_b(t) &= a_\beta + b_\beta \cos(2\pi t/T_b - \phi_\beta), & \tilde{\gamma}_b(t) &= a_\gamma + b_\gamma \cos(2\pi t/T_b - \phi_\gamma).\end{aligned}\quad [\text{S18}]$$

Every Fourier coefficient is taken as an independent parameter except those of $\tilde{\zeta}_b$, since the condition in Eq. S15 imposes $a_\zeta = -b_\zeta \cos(\phi_\zeta)$.

To obtain values for the parameters in Eq. S17, we fit our model to experimental data. We track the centroid and the orientation of the cell body's segmented image. Given the ellipsoidal symmetry of the cell, we interpret these data respectively as $\Pi\mathbf{c}$ and θ , where $\Pi\mathbf{k} = (\cos\theta, \sin\theta)$. Image segmentation of the eyespot give us the tracking data for $\Pi\mathbf{e}$. As in the main text, we denote by Π the projection on the focal plane. From Eqs. S13, S14, and S16 we have that

$$\begin{aligned}\theta(t) &= \theta_n - \arctan(\sin\alpha(t) \tan\beta(t)), \\ \Pi\mathbf{c}(t) &= \begin{pmatrix} o_y \\ o_z \end{pmatrix} + \begin{pmatrix} \sin\theta_n \\ -\cos\theta_n \end{pmatrix} \rho(t) \sin\psi(t) + \begin{pmatrix} \cos\theta_n \\ \sin\theta_n \end{pmatrix} \zeta(t), \\ \Pi\mathbf{e}(t) &= \Pi\mathbf{i}(t)e_i + \Pi\mathbf{k}(t)e_k + \Pi\mathbf{c}(t)\end{aligned}\quad [\text{S19}]$$

where

$$\begin{aligned}\Pi\mathbf{i} &= \begin{pmatrix} \sin\theta_n \\ -\cos\theta_n \end{pmatrix} (\sin\alpha \cos\beta \cos\gamma + \cos\alpha \sin\gamma) - \begin{pmatrix} \cos\theta_n \\ \sin\theta_n \end{pmatrix} \sin\beta \cos\gamma \\ \text{and } \Pi\mathbf{k} &= \begin{pmatrix} \sin\theta_n \\ -\cos\theta_n \end{pmatrix} \sin\alpha \sin\beta + \begin{pmatrix} \cos\theta_n \\ \sin\theta_n \end{pmatrix} \cos\beta.\end{aligned}$$

From all of the definitions above, we obtain the expressions $\theta(\xi, t)$, $\Pi\mathbf{c}(\xi, t)$, and $\Pi\mathbf{e}(\xi, t)$ of our measured quantities in terms of the kinematic parameters ξ . We then obtain an estimate of the parameters ξ in three steps.

The quantities θ , $\Pi\mathbf{c}$, and $\Pi\mathbf{e}$ depend on subsets of ξ , which we denote by ξ_θ , ξ_c , and ξ_e , respectively. We first calculate the subset of nine parameters $\xi_I := \xi_\theta$. Written in full,

$$\xi_I = \{T_b, \theta_n, \Delta\psi, a_\alpha, b_\alpha, \phi_\alpha, a_\beta, b_\beta, \phi_\beta\}.$$

We obtain an estimate ξ_I^* of such parameters by solving numerically the following minimization problem:

$$\xi_I^* = \operatorname{argmin}_{\xi_I} \sum_j \left| \theta(\xi_I, t_j^\theta) - \theta^*(t_j^\theta) \right|^2. \quad [\text{S20}]$$

In the right-hand side of Eq. S20 we have denoted with an asterisk the tracking data, and by $\{t_j^\theta\}$ the time instants where tracking data are available (analogous notation is used systematically in the following). The second subset of parameters we calculate is the difference between sets $\xi_{II} := \xi_c \setminus \xi_I$, which consists of 11 elements:

$$\xi_{II} = \{\mathbf{o}_h, \Delta\zeta, a_\rho, b_\rho, \phi_\rho, a_\psi, b_\psi, \phi_\psi, b_\zeta, \phi_\zeta\}.$$

We obtain an estimate ξ_{II}^* of these parameters by solving

$$\xi_{II}^* = \operatorname{argmin}_{\xi_{II}} \sum_j \|\Pi\mathbf{c}(\xi_{II}, \xi_I^*, t_j^c) - \Pi\mathbf{c}^*(t_j^c)\|^2. \quad [\text{S21}]$$

Finally, the last subset of five parameters,

$$\xi_{III} = \{e_i, e_k, a_\gamma, b_\gamma, \phi_\gamma\},$$

where $\xi_{III} := \xi_e \setminus (\xi_I \cup \xi_{II})$, is calculated by solving

$$\xi_{III} = \operatorname{argmin}_{\xi_{III}} \sum_j \|\Pi\mathbf{e}(\xi_{III}, \xi_{II}^*, \xi_I^*, t_j^e) - \Pi\mathbf{e}^*(t_j^e)\|^2. \quad [\text{S22}]$$

Collecting the results from Eqs. S20–S22 we obtain all the parameters $\xi^* = \xi_I^* \cup \xi_{II}^* \cup \xi_{III}^*$ needed to fully reconstruct the time evolution of \mathbf{c} and \mathbf{R} . The three-step fitting procedure is devised to minimize the number of parameters to be calculated at every step. The eyespot tracking data are only needed to recover 5 parameters (out of 25). The data for $\Pi\mathbf{e}$ are fewer than the ones for $\Pi\mathbf{c}$ and θ (41 to 48 data points, depending on the experiment), but they always outnumber the free parameters to be calculated.

We end this section with a few comments. First, notice that θ depends only on the Euler angles α and β (Eq. S19). Solving Eq. S22 is then crucial to find the third angle γ , which enables us to recover the rotation \mathbf{R} (see the discussion in the main text). Second, from Eq. S19 we have that $\Pi\mathbf{c}$ and θ are invariant under the transformations $\psi \mapsto \pi - \psi$ and $\alpha \mapsto \pi - \alpha$, respectively. This ultimately leads to an ambiguity on the sign of $\Delta\psi$, which in turn determines the sign of the angle γ . The two cases correspond to one motion of the moving frame and to its reflection with respect to the focal plane. In our experiments, the choice of the sign of $\Delta\psi$ was based on a visual check on the motion of the eyespot during rotation (exploiting the opacity of the cell). Rotation direction is further confirmed by its consistency with the out-of-plane motion of tracer particles near cells' bodies, which we estimated through their image changes induced by defocusing and optical aberrations (32).

3. Reconstruction of the Flagellar Shapes: Implementation Details

As stated in the main text we have, for every phase $\tau \in [0, T_b]$, a set of N_{pl} planes, each of which contains a set of points where we can locate the flagellum projection. For every plane $j = 1, \dots, N_{pl}$, we denote by P_j^* the set of experimental points and by N_j the number of points in the set. We denote by \mathbf{p}_{ij}^* the points in P_j^* , with $i = 1, \dots, N_j$. With the definitions given in the main text, the expression for the projection error in Eq. 3 becomes

$$Err(\mathbf{r}) = \sum_{j=1}^{N_{pl}} \sum_{i=1}^{N_j} \text{dist}(\mathbf{p}_{ij}^*, \Pi_j \mathbf{r})^2 = \min_{\{s_{ij}\}} \sum_{j=1}^{N_{pl}} \sum_{i=1}^{N_j} \|\mathbf{p}_{ij}^* - \Pi_j \mathbf{r}(s_{ij}^i)\|^2,$$

where \mathbf{r} is a 3D curve. A curve \mathbf{r} describes the flagellum (at phase τ) if it minimizes the projection error. To find the flagellum we take $\mathbf{r}(s) = Sp(s; \mathbf{x}_1, \dots, \mathbf{x}_{N_{sp}})$ as in Eq. 4, where Sp is a cubic spline defined for $s \in [0, 1]$ and interpolating N_{sp} points $\mathbf{x}_1, \dots, \mathbf{x}_{N_{sp}}$. The nodes relative to the interpolation points are equispaced on $[0, 1]$. The starting point \mathbf{x}_1 , determining the flagellum attachment with the ellipsoidal body, is the same for every flagellar phase, and it is fixed a priori. We solve numerically

$$\underset{\{s_{ij}\}, \mathbf{x}_1, \dots, \mathbf{x}_{N_{sp}}}{\text{argmin}} \sum_{j=1}^{N_{pl}} \sum_{i=1}^{N_j} \|\mathbf{p}_{ij}^* - \Pi_j Sp(s_{ij}; \mathbf{x}_1, \dots, \mathbf{x}_{N_{sp}})\|^2 \quad [\text{S23}]$$

to find the remaining interpolation points $\mathbf{x}_2, \dots, \mathbf{x}_{N_{sp}}$, together with the auxiliary variables s_{ij} . We allow for the number N_{sp} of interpolating points to vary from phase to phase. Similarly, we allow for the boundary conditions to vary from phase to phase, in order for the minimization algorithm to converge. We do not impose constraints on the length of the curve \mathbf{r} , which is an outcome of the algorithm. As a result, lengths tend to vary slightly for different phases.

4. Uncertainties of the Reconstruction Procedure and Variability of Results

We report here the results of our body kinematics reconstruction for six different experimental datasets. Three of them, denoted Cell1a*, Cell1b, and Cell1c, correspond to the same specimen (Cell1) observed at different times (a, b, and c). The dataset Cell1a* is the one we relied on for the results presented in the main text. The other three datasets, denoted Cell2, Cell3, and Cell4, correspond to three different cells (so, four different specimens in total are analyzed).

The resulting best fits of our kinematic model for each set are shown in Fig. S2, superimposed on experimental data. Tables S1–S3 present the results of the three-step fitting procedure described in *Supporting Information*, section 2. Values of the fitted parameters are reported together with their relative (95%) confidence bounds. All fits are obtained on time intervals in which the cell completes one turn of its helical trajectory (while our observations cover typically approximately three turns).

Comparing different observations a, b, and c of the same specimen (Cell1), the motion characteristics are quite reproducible (although some variability emerges). Some kinematic quantities are also common to different specimens. All of the helical trajectories observed are quite narrow (see the average radius a_ρ). The beating period T_b oscillates around 25 ms. Also, the displacement Δz after one beat along the helix axis shows small variability. This is not quite the case for the body rotation angle after one beat $\Delta\psi$. As a consequence, the total number $N = 2\pi/\Delta\psi$ of beats needed to close a full body rotation (or, equivalently, a turn of the helical trajectory) varies from $N \approx 21$ for Cell1a* to $N \approx 35$ for Cell4. Interestingly, however, we always recover positive values for $\Delta\psi$. That is, cells always appear to rotate clockwise.

We also report the results of one additional flagellar beat reconstruction. Fig. S3 shows a comparison between the reconstructed flagellar shapes of Cell1a* and those of Cell2. This allows us to appreciate in 3D an example of the (slight) variability of the flagellar beat between cells, but also the consistency of the flagellar beating style. The uncertainties of our reconstruction procedure (for both Cell1a* and Cell2) are quantified by confidence intervals. Tables S4 and S5 present the confidence intervals for the interpolation points' coordinates of the splines that describe the flagellum (we also report the different estimated lengths of the flagellum at each phase; cf. *Supporting Information*, section 2). While most of the confidence intervals are quite narrow, some of them reveal large uncertainties. This is due to the occasional scarcity of experimental data, leading to divergent values of the confidence bounds, which are, however, confined to some small portion of the flagellum, at one particular phase.

The reconstructed flagellum of Cell1a* is compared with the experimental data in Fig. S4. For both flagellar reconstructions we consider data from a time range of ~ 21 beats. In the case of Cell1a* this corresponds to one complete turn of the helical trajectory, while for Cell2 it corresponds to *ca.* three-quarters of a turn.

We give an estimate of the variability of the flagellar beat among different observations also in a more quantitative way. We use the reconstructed 3D flagellar shapes of Cell1a* and the image data from the other five datasets. The reconstructed time history of flagellar shapes from Cell1a*, conveniently scaled in both space and time, is attached to the other cells' bodies (we use here our results from the body kinematics reconstruction). Then, the projections on the focal plane of these flagellar shapes are superimposed on the experimental images (Fig. S5 and Movie S4). A good overlap clearly emerges, showing that Cell1a* is a valid representative of a common beating style. To make the comparison quantitative we calculate the "standard projective error" σ between the reconstructions and the experimental data. The error σ is defined as follows. We consider time intervals spanning $\gtrsim 20$ flagellar beats. For each time frame in the interval, we obtain from the segmentation of microscopy images a set of points where the projection of the cell flagellum is visible. We then calculate the distances $\{d_i\}$ of each point to the projection of the reconstructed flagellum. The standard projection error is then defined as

$$\sigma = \sqrt{\frac{\sum_i d_i^2}{N_{pts}}},$$

where N_{pts} is the total number of points considered. The standard projection errors for each dataset (given in terms of percentage of the flagellar length) are reported in Fig. S5 and range between 2.1% and 8.9%.

5. Physical Consistency Test for the Reconstructed Kinematics

In the present section we show that our kinematics reconstruction is consistent with the underlying physics of the system, namely, low Reynolds number hydrodynamics. We use the reconstructed flagellar shapes from Cell1a* (conveniently regularized) to calculate the body motion that results if we impose the force and torque balance (Eq. S3). We then compare the calculated motion with the one recorded in the experiments.

We rely on some simplifying assumptions. The hydrodynamic forces acting on the flagellum are calculated using RFT (9). With this hypothesis, the viscous force acting on the flagellum depends on two “resistive” coefficients, C_{\perp} and C_{\parallel} . More precisely, the linear density force $\mathbf{f}(s, t)$ acting on the point of the flagellum $\mathbf{r}(s, t)$ at time t and arc length s is given by

$$\mathbf{f}(s, t) = -C_{\perp}\mathbf{v}_{\perp}(s, t) - C_{\parallel}\mathbf{v}_{\parallel}(s, t),$$

where $\mathbf{v}_{\parallel}(s, t) = \frac{\partial \mathbf{r}}{\partial s}(s, t) \cdot \frac{\partial \mathbf{r}}{\partial t}(s, t)$ and $\mathbf{v}_{\perp}(s, t) = \frac{\partial \mathbf{r}}{\partial t}(s, t) - \mathbf{v}_{\parallel}(s, t)$ are the local velocity components parallel and perpendicular to the flagellum. The total viscous force \mathbf{f}_{flag} and torque \mathbf{g}_{flag} acting on the flagellum are then given by

$$\mathbf{f}_{flag} = \int_0^L \mathbf{f}(s, t) ds \quad \text{and} \quad \mathbf{g}_{flag} = \int_0^L (\mathbf{r}(s, t) - \mathbf{c}(t)) \times \mathbf{f}(s, t) ds.$$

Resistive coefficients are known to depend heavily on the geometry of the flagellum and on its hydrodynamic interaction with external structures. No theoretical choice is available for something that resembles our case, where the flagellum beats in close proximity to the *Euglena*'s body. To get a reasonable choice for the resistive coefficients, following ref. 9, we calculate them as those which best fit the experimental data. We explain this in more detail below.

We consider the total viscous force \mathbf{f} and torque \mathbf{g} acting on the swimmer as given by

$$\mathbf{f} = \mathbf{f}_{body} + \mathbf{f}_{flag} \quad \text{and} \quad \mathbf{g} = \mathbf{g}_{body} + \mathbf{g}_{flag},$$

where \mathbf{f}_{body} and \mathbf{g}_{body} are the total force and torque acting on an ellipsoid of the same size of Cell1 (moving in an unbounded fluid). The expressions for \mathbf{f}_{body} and \mathbf{g}_{body} can be commonly found in the literature (see e.g., ref. 31). Imposing the force and torque balance Eq. S3, we then obtain an expression of the type S6, where the right-hand side depends only on our flagellar beat reconstruction. This allows us to calculate the velocities $\bar{\mathbf{v}}(C_{\perp}, C_{\parallel}, t)$ and $\bar{\boldsymbol{\omega}}(C_{\perp}, C_{\parallel}, t)$ (definitions and notations taken from *Supporting Information*, section 1). Denoting by $\bar{\mathbf{v}}^*(t)$ and $\bar{\boldsymbol{\omega}}^*(t)$ the velocities that we obtain from our experiments, we define the optimal coefficients as

$$(C_{\perp}^*, C_{\parallel}^*) = \operatorname{argmin}_{C_{\perp}, C_{\parallel}} \int_0^{T_b} \nu_1 \|\bar{\mathbf{v}}(C_{\perp}, C_{\parallel}, t) - \bar{\mathbf{v}}^*(t)\|^2 + \nu_2 \|\bar{\boldsymbol{\omega}}(C_{\perp}, C_{\parallel}, t) - \bar{\boldsymbol{\omega}}^*(t)\|^2 dt$$

for conveniently chosen normalization constants ν_1 and ν_2 . We take the velocities $\bar{\mathbf{v}}(C_{\perp}^*, C_{\parallel}^*, t)$ and $\bar{\boldsymbol{\omega}}(C_{\perp}^*, C_{\parallel}^*, t)$ as the ones that best describe the kinematics generated by the flagellar beat under the hydrodynamic force balance condition. Rotations and translations of the cell body are then calculated by time integration (S7). The velocities and trajectories that we obtain from the flagellar beat are compared with the experimental ones in Fig. S6.

We have a qualitative agreement (which confirms that the time sequence of reconstructed flagellar shapes is consistent with the observed swimming motion) but we are not able to reproduce all observations in full quantitative detail. Moreover, we emphasize that our estimates for the optimal resistive coefficients lead to quite nonstandard values. Indeed, if we compare them with those measured for sperm cells' flagella swimming in free space (9) our value for $C_{\perp}^* \approx 3.1 \text{ fN s } \mu\text{m}^{-2}$ is *ca.* 2.5 times larger and the ratio $C_{\perp}^*/C_{\parallel}^* \approx 21.7$ is slightly more than one order of magnitude larger. This large discrepancy, however, is not too surprising in view of theoretical studies (33) on resistive coefficients for flagella near boundaries and of the fact that the large cell body can be seen as a (moving) wall near the beating flagellum. Clearly, our analysis represents a very crude way to encode the nonlocal hydrodynamic interactions between flagellum and cell body, and a more detailed study will be necessary in the future.

As a final remark, it is worth noticing that the values of the optimal resistive coefficients are compatible with those of a smooth flagellum. This is not a trivial outcome. The *Euglena*'s flagellum, like that of most algae, is not smooth but it is rather coated with thin, hair-like structures called mastigonemes (29). Stiff (tubular) mastigonemes are known to affect flagellar thrust in a major way, to the point of inverting the direction of resulting body motion. For example, the flagellum of *Ochromonas malhamensis* propels the cell in the same direction of the one of flagellar wave propagation (30). This does not seem to happen in the case of euglenid flagellar swimming, as can be inferred by comparing body velocities and flagellar shape evolution (Movie S5). When the flagellar wave propagates parallel to the major axis of the body we observe a peak in the translational velocity of the cell in the opposite direction (light-red to black phases in Fig. 5E). During the swing around the body (red to dark-blue phases), the cell counterrotates, and the angular velocity peaks. Both angular and translational velocities decrease when a wave is fading at the distal end of the flagellum, and a new one is emerging from the cell body attachment.

It has been conjectured (29) that the soft (nontubular) mastigonemes of the euglenid flagellum do not invert the flagellar thrust mechanism. Our results provide further evidence to support this claim.

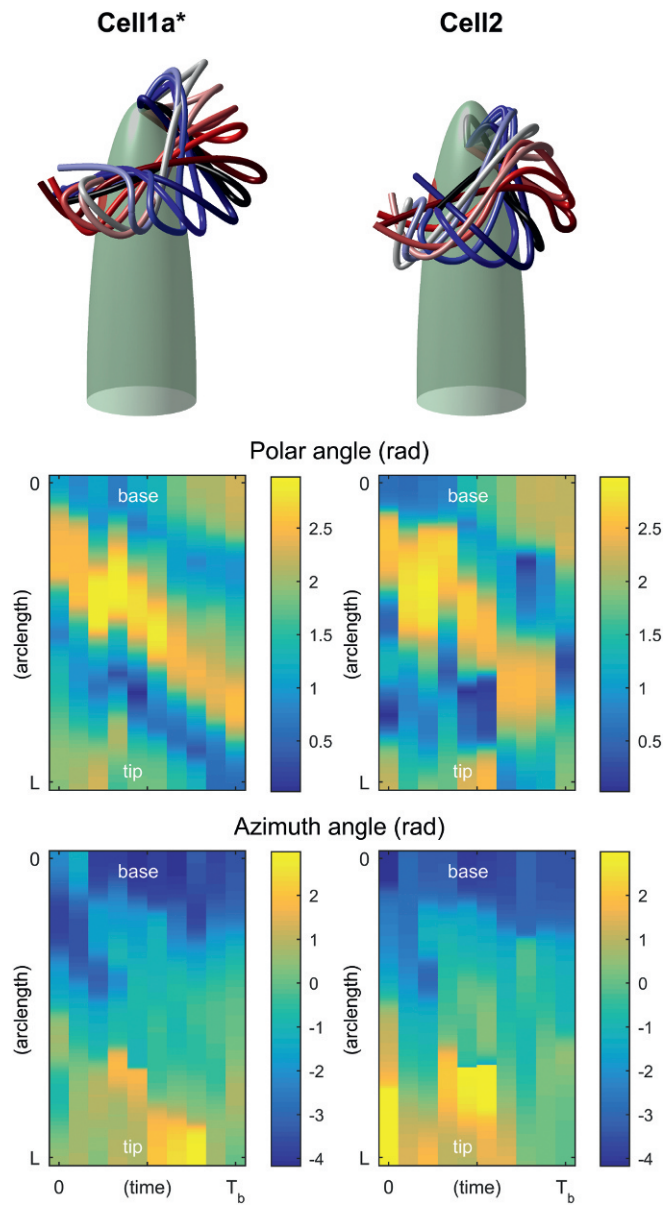


Fig. S3. Comparison between the reconstructed flagellar shapes for Cell1a* (*Left*) and Cell2 (*Right*). Sequence of flagella during the 10 phases (*Top*). Polar angle (*Middle*) and azimuth angle (*Bottom*) of the unit tangent vector to the flagella, as functions of arc length and time.

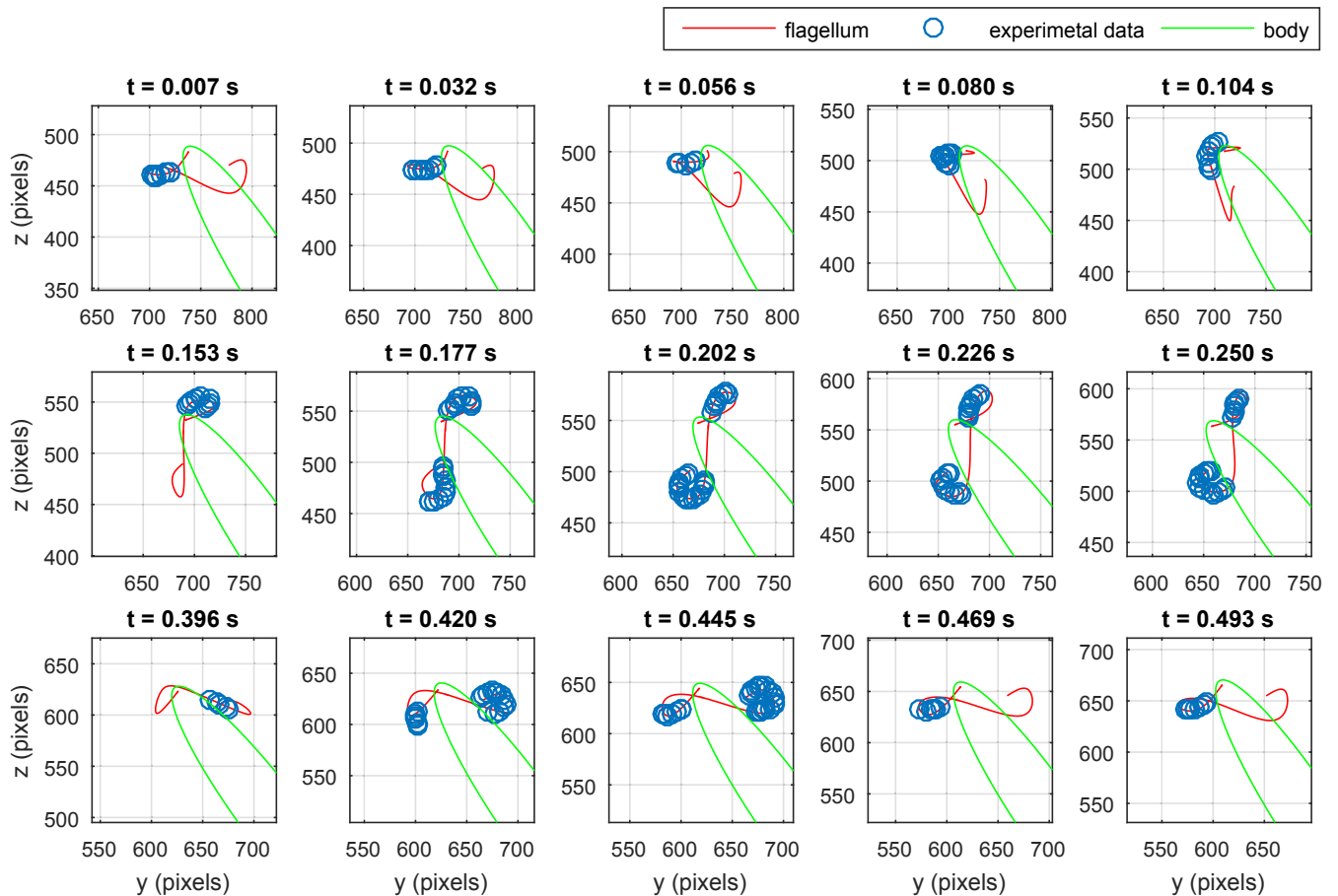


Fig. S4. Frames taken at times $t_k = \tau + kT_b$ for a fixed phase τ . The flagellum lies in the same configuration with respect to the body frame but is seen from different viewpoints. Images show the projection of the reconstructed flagellar shape (in red) superimposed on experimental data (blue circles).

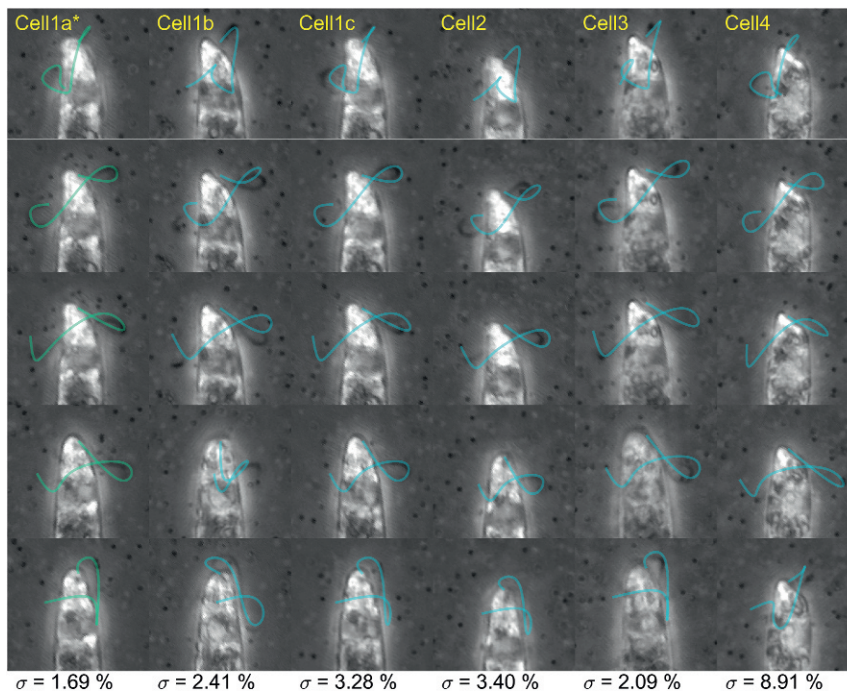


Fig. S5. The reconstructed flagellum from Cell1a* (green), conveniently scaled in both space and time, is superimposed on experimental images from other trials (blue). The standard projection error σ is also shown.

Table S1. Parameter values with confidence bounds obtained by fitting θ

| Parameter | Parameter value ($\pm 95\%$ confidence bounds) | | | | | |
|-----------------------|---|--------------------|--------------------|--------------------|--------------------|--------------------|
| | Cell1a* | Cell1b | Cell1c | Cell2 | Cell3 | Cell4 |
| θ_n , rad | 2.18 (1.6e-04) | 1.97 (1.5e-04) | 0.60 (1.9e-04) | 5.27 (1.8e-04) | 2.28 (2.8e-04) | 3.95 (3.3e-04) |
| $\Delta\psi$, rad | 0.30 (4.8e-04) | 0.33 (4.0e-04) | 0.33 (5.5e-04) | 0.22 (1.9e-04) | 0.25 (5.9e-04) | 0.18 (4.1e-04) |
| T_b , ms | 24.30 (6.4e-03) | 25.28 (9.1e-03) | 23.84 (9.2e-03) | 25.49 (4.7e-03) | 24.89 (6.8e-03) | 27.99 (8.2e-03) |
| a_{α} , rad | 3.44 (1.2e-02) | 5.21 (2.1e-02) | 2.16 (3.8e-02) | 2.90 (3.0e-03) | 0.75 (2.6e-02) | 3.07 (1.9e-02) |
| b_{α} , rad | 0.22 (3.1e-03) | 0.20 (3.2e-03) | 0.25 (4.4e-03) | 0.18 (2.3e-03) | 0.18 (2.7e-03) | 0.10 (2.8e-03) |
| ϕ_{α} , rad | 5.48 (4.3e-02) | 4.50 (1.2e-01) | 2.22 (1.7e-01) | 2.68 (2.0e-02) | 0.28 (7.4e-02) | 0.21 (9.0e-02) |
| a_{β} , rad | 0.08 (1.8e-04) | 0.09 (2.1e-04) | 0.08 (2.7e-04) | 0.16 (2.6e-04) | 0.10 (2.2e-04) | 0.12 (2.7e-04) |
| b_{β} , rad | 0.02 (2.5e-04) | 0.02 (3.0e-04) | 0.02 (3.7e-04) | 0.03 (3.7e-04) | 0.02 (2.7e-04) | 0.01 (3.4e-04) |
| ϕ_{β} , rad | 0.57 (3.8e-02) | 5.86 (1.1e-01) | 3.82 (1.7e-01) | 4.52 (2.3e-02) | 1.86 (7.5e-02) | 1.29 (9.2e-02) |

Table S2. Parameter values with confidence bounds obtained by fitting Πc

| Parameter | Parameter value ($\pm 95\%$ confidence bounds) | | | | | |
|----------------------------|---|---------------------|--------------------|---------------------|---------------------|---------------------|
| | Cell1a* | Cell1b | Cell1c | Cell2 | Cell3 | Cell4 |
| h_y , μm | 138.78 (1.3e-02) | 150.11 (1.5e-02) | 28.92 (5.8e-02) | 84.47 (5.6e-03) | 147.47 (2.4e-02) | 143.76 (2.0e-02) |
| h_z , μm | 36.02 (1.7e-02) | 30.49 (3.4e-02) | 47.88 (4.0e-02) | 106.61 (7.8e-03) | 51.43 (2.7e-02) | 111.92 (2.1e-02) |
| Δz , μm | 1.72 (8.2e-04) | 1.66 (7.2e-04) | 1.79 (1.0e-03) | 1.39 (4.4e-04) | 1.74 (8.1e-04) | 1.66 (5.6e-04) |
| a_{ρ} , μm | 0.75 (7.1e-03) | 0.55 (5.5e-03) | 0.47 (7.9e-03) | 0.47 (5.1e-03) | 0.42 (8.5e-03) | 1.17 (8.2e-03) |
| b_{ρ} , μm | 0.20 (1.0e-02) | 0.20 (7.8e-03) | 0.21 (1.1e-02) | 0.24 (7.3e-03) | 0.19 (1.2e-02) | 0.18 (1.2e-02) |
| ϕ_{ρ} , rad | 5.83 (4.9e-02) | 5.18 (4.0e-02) | 4.44 (5.4e-02) | 5.55 (3.0e-02) | 2.55 (6.4e-02) | 1.08 (6.6e-02) |
| a_{ψ} , rad | 4.76 (1.0e-02) | 6.16 (1.1e-02) | 1.68 (1.9e-02) | 1.55 (1.3e-02) | 0.08 (2.3e-02) | 3.40 (7.1e-03) |
| b_{ψ} , rad | 0.26 (1.3e-02) | 0.27 (1.4e-02) | 0.43 (2.4e-02) | 0.47 (1.5e-02) | 0.46 (2.8e-02) | 0.09 (9.8e-03) |
| ϕ_{ψ} , rad | 3.95 (5.4e-02) | 3.44 (5.7e-02) | 2.67 (6.2e-02) | 4.18 (3.8e-02) | 0.92 (7.1e-02) | 6.12 (1.1e-01) |
| b_z , μm | 0.24 (7.1e-03) | 0.25 (5.5e-03) | 0.21 (7.9e-03) | 0.19 (5.1e-03) | 0.26 (8.5e-03) | 0.20 (8.2e-03) |
| ϕ_z , rad | 0.01 (3.0e-02) | 5.21 (2.2e-02) | 2.70 (3.7e-02) | 3.47 (2.7e-02) | 0.83 (3.3e-02) | 1.73 (4.1e-02) |

Table S3. Parameter values with confidence bounds obtained by fitting IIe

| Parameter | Parameter value ($\pm 95\%$ confidence bounds) | | | | | |
|---------------------------|---|--------------------|--------------------|--------------------|--------------------|--------------------|
| | Cell1a* | Cell1b | Cell1c | Cell2 | Cell3 | Cell4 |
| $e_k, \mu\text{m}$ | 16.98 (9.1e-03) | 16.72 (1.8e-02) | 16.73 (1.2e-02) | 14.45 (1.5e-02) | 17.74 (1.1e-02) | 17.55 (1.5e-02) |
| $e_r, \mu\text{m}$ | 1.71 (4.8e-02) | 2.66 (9.3e-02) | 3.50 (5.5e-02) | 2.19 (1.1e-01) | 2.81 (8.5e-02) | 2.99 (1.1e-01) |
| a_γ, rad | 0.56 (2.6e-02) | 0.84 (2.1e-02) | 1.43 (1.6e-02) | 1.23 (3.7e-02) | 1.00 (4.2e-03) | 0.31 (5.2e-03) |
| b_γ, rad | 0.23 (1.1e-02) | 0.21 (1.2e-02) | 0.28 (6.8e-03) | 0.20 (1.1e-02) | 0.19 (5.4e-03) | 0.10 (4.2e-03) |
| ϕ_γ, rad | 2.21 (4.5e-02) | 1.14 (5.3e-02) | 5.32 (2.6e-02) | 5.72 (6.0e-02) | 3.21 (2.7e-02) | 3.41 (4.1e-02) |

Table S4. Uncertainties of the flagellar shapes reconstruction procedure for Cell1a*

| n_{sp} | Beat phase | | | | | | | | | |
|----------|--|----------|----------|----------|----------|----------|----------|----------|----------|----------|
| | $0.0T_b$ | $0.1T_b$ | $0.2T_b$ | $0.3T_b$ | $0.4T_b$ | $0.5T_b$ | $0.6T_b$ | $0.7T_b$ | $0.8T_b$ | $0.9T_b$ |
| | $\pm 95\%$ confidence bounds for i-components, μm | | | | | | | | | |
| 1 | 0.00 | 0.00 | 0.00 | 0.00 | 0.00 | 0.00 | 0.00 | 0.00 | 0.00 | 0.00 |
| 2 | 0.35 | 0.32 | 0.18 | 0.12 | 0.10 | 0.27 | 0.26 | 0.31 | 0.13 | 0.22 |
| 3 | 0.19 | 0.16 | 0.06 | 0.03 | 0.05 | 0.10 | 0.11 | 0.19 | 0.25 | 0.33 |
| 4 | 0.28 | 0.32 | 0.07 | 0.08 | 0.18 | 0.24 | 0.37 | 0.38 | 0.67 | 0.54 |
| 5 | 1.18 | 0.37 | 0.14 | 0.42 | 0.14 | 0.31 | 0.24 | 0.46 | 0.17 | 0.17 |
| 6 | 0.77 | 0.09 | 0.27 | 1.07 | 0.33 | 0.63 | 0.13 | 0.18 | 0.24 | 0.25 |
| 7 | 0.09 | | 0.19 | 2.84 | 1.53 | | 0.13 | 0.13 | | |
| 8 | | | | 322.35 | | | | 0.14 | | |
| 9 | | | | 2,071.27 | | | | | | |
| | $\pm 95\%$ confidence bounds for j-components, μm | | | | | | | | | |
| 1 | 0.00 | 0.00 | 0.00 | 0.00 | 0.00 | 0.00 | 0.00 | 0.00 | 0.00 | 0.00 |
| 2 | 0.29 | 0.21 | 0.18 | 0.07 | 0.08 | 0.28 | 0.16 | 0.46 | 0.17 | 0.18 |
| 3 | 0.25 | 0.17 | 0.08 | 0.12 | 0.10 | 0.13 | 0.29 | 0.16 | 0.19 | 0.21 |
| 4 | 0.27 | 0.22 | 0.10 | 0.12 | 0.14 | 0.10 | 0.28 | 0.27 | 0.17 | 0.34 |
| 5 | 1.40 | 0.36 | 0.06 | 0.66 | 0.10 | 0.13 | 0.17 | 0.19 | 0.26 | 0.43 |
| 6 | 0.47 | 0.23 | 0.37 | 0.20 | 0.29 | 1.00 | 0.13 | 0.17 | 0.29 | 0.36 |
| 7 | 0.29 | | 0.22 | 9.69 | 1.35 | | 0.21 | 0.13 | | |
| 8 | | | | 174.70 | | | | 0.13 | | |
| 9 | | | | 1,051.48 | | | | | | |
| | $\pm 95\%$ confidence bounds for k-components, μm | | | | | | | | | |
| 1 | 0.00 | 0.00 | 0.00 | 0.00 | 0.00 | 0.00 | 0.00 | 0.00 | 0.00 | 0.00 |
| 2 | 0.42 | 0.31 | 0.11 | 0.07 | 0.08 | 0.09 | 0.04 | 0.07 | 0.05 | 0.12 |
| 3 | 0.19 | 0.22 | 0.19 | 0.21 | 0.12 | 0.11 | 0.12 | 0.18 | 0.05 | 0.13 |
| 4 | 0.34 | 0.27 | 0.10 | 0.55 | 0.24 | 0.10 | 0.41 | 0.05 | 0.52 | 0.33 |
| 5 | 0.25 | 0.07 | 0.16 | 0.10 | 0.32 | 0.11 | 0.09 | 0.36 | 0.13 | 0.33 |
| 6 | 0.40 | 0.08 | 0.10 | 2.80 | 0.09 | 0.11 | 0.09 | 0.07 | 0.09 | 0.15 |
| 7 | 0.08 | | 0.16 | 0.09 | 0.23 | | 0.07 | 0.11 | | |
| 8 | | | | 161.13 | | | | 0.06 | | |
| 9 | | | | 1,080.15 | | | | | | |
| | Flagellar length, μm | | | | | | | | | |
| | 38.9 | 39.1 | 37.9 | 38.7 | 36.5 | 40.1 | 36.9 | 35.7 | 37.7 | 39.6 |

Confidence bounds for the interpolation points' coordinates of the splines that describe the flagellum (at each phase) and estimated flagellar length.

Table S5. Uncertainties of the flagellar shapes reconstruction procedure for Cell2

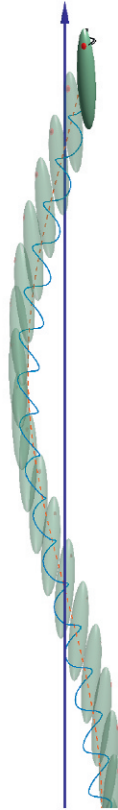
| n_{sp} | Beat phase | | | | | | | | | |
|--|------------|----------|----------|----------|----------|----------|----------|----------|----------|----------|
| | $0.0T_b$ | $0.1T_b$ | $0.2T_b$ | $0.3T_b$ | $0.4T_b$ | $0.5T_b$ | $0.6T_b$ | $0.7T_b$ | $0.8T_b$ | $0.9T_b$ |
| ±95% confidence bounds for i-components, μm | | | | | | | | | | |
| 1 | 0.00 | 0.00 | 0.00 | 0.00 | 0.00 | 0.00 | 0.00 | 0.00 | 0.00 | 0.00 |
| 2 | 0.39 | 0.14 | 0.09 | 0.08 | 0.06 | 0.10 | 0.22 | 0.09 | 0.13 | 0.30 |
| 3 | 0.17 | 0.19 | 0.37 | 0.45 | 0.09 | 0.26 | 0.35 | 0.07 | 0.11 | 0.18 |
| 4 | 0.51 | 2.61 | 0.49 | 0.25 | 0.44 | 0.42 | 0.43 | 0.19 | 0.42 | 0.24 |
| 5 | 0.53 | 3.80 | 0.39 | 0.59 | 0.09 | 0.15 | 0.26 | 0.26 | 1.02 | 0.75 |
| 6 | 4.57 | | 0.16 | 1.45 | 0.14 | 0.19 | | | | |
| 7 | 58.23 | | 0.43 | | 0.14 | | | | | |
| ±95% confidence bounds for j-components, μm | | | | | | | | | | |
| 1 | 0.00 | 0.00 | 0.00 | 0.00 | 0.00 | 0.00 | 0.00 | 0.00 | 0.00 | 0.00 |
| 2 | 0.30 | 0.13 | 0.24 | 0.13 | 0.11 | 0.33 | 0.78 | 0.25 | 0.23 | 0.27 |
| 3 | 0.38 | 0.56 | 0.73 | 0.25 | 0.13 | 0.29 | 0.75 | 0.20 | 0.16 | 0.32 |
| 4 | 0.24 | 0.49 | 0.87 | 0.14 | 0.10 | 0.39 | 0.85 | 0.23 | 0.63 | 0.34 |
| 5 | 2.35 | 20.72 | 0.31 | 0.89 | 0.10 | 0.20 | 0.93 | 0.70 | 1.57 | 1.00 |
| 6 | 4.16 | | 0.13 | 1.37 | 0.11 | 0.25 | | | | |
| 7 | 21.80 | | 0.38 | | 0.34 | | | | | |
| ±95% confidence bounds for k-components, μm | | | | | | | | | | |
| 1 | 0.00 | 0.00 | 0.00 | 0.00 | 0.00 | 0.00 | 0.00 | 0.00 | 0.00 | 0.00 |
| 2 | 0.71 | 0.25 | 0.22 | 0.13 | 0.05 | 0.08 | 0.16 | 0.08 | 0.08 | 0.18 |
| 3 | 0.26 | 0.60 | 1.87 | 0.29 | 0.13 | 0.19 | 0.23 | 0.07 | 0.06 | 0.33 |
| 4 | 0.77 | 2.51 | 0.79 | 0.47 | 0.40 | 0.63 | 0.41 | 0.12 | 0.25 | 0.11 |
| 5 | 1.80 | 0.83 | 0.16 | 0.25 | 0.18 | 0.27 | 0.89 | 0.12 | 0.16 | 0.21 |
| 6 | 4.37 | | 0.17 | 0.37 | 0.15 | 0.17 | | | | |
| 7 | 47.88 | | 0.12 | | 0.12 | | | | | |
| Flagellar length, μm | | | | | | | | | | |
| | 35.3 | 34.5 | 31.4 | 29.4 | 34.1 | 38.8 | 37.5 | 35.4 | 34.9 | 36.2 |

Confidence bounds for the interpolation points' coordinates of the splines that describe the flagellum (at each phase) and estimated flagellar length.



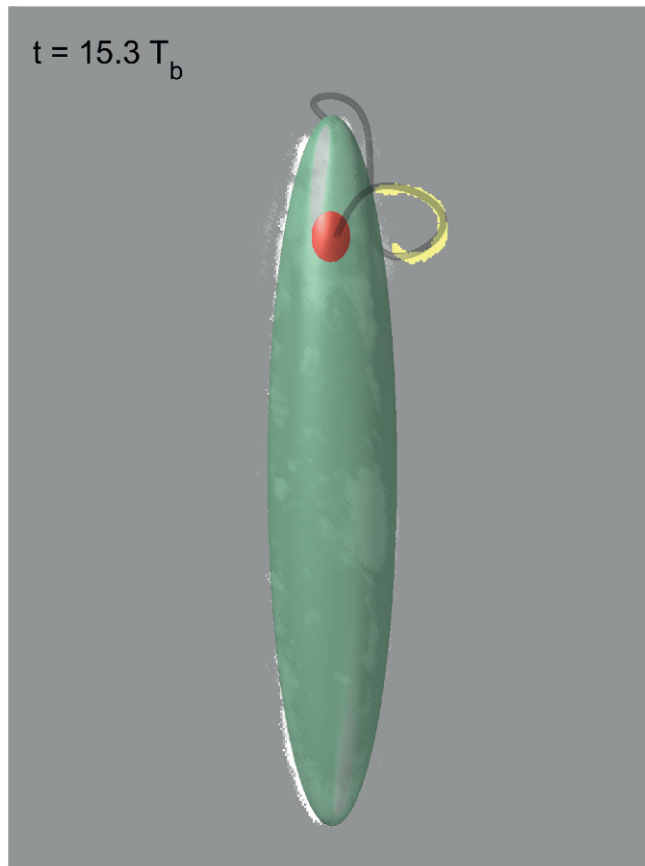
Movie S1. Montage of video recordings of swimming *E. gracilis* observed under a microscope (at increasing magnification and image-acquisition rate). At time scales larger than the flagellar beating period cells can be observed moving on a helical path while rotating about a fixed axis. At smaller time scales, finer features of the rototraslatory motion appear.

[Movie S1](#)



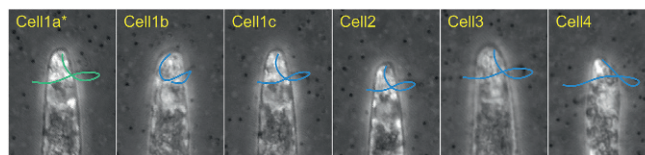
Movie S2. Reconstructed swimming kinematics of *E. gracilis*. The resulting trajectory of the cell can be seen as a smooth circular helix (the "backbone" trajectory), perturbed by periodic "swirls" at the flagellar beating time scale. The cell completes one turn of the helix while undergoing a full rotation around the axis of the helix. The *Euglena*'s body is not to scale with the displacements for visualization purposes.

[Movie S2](#)



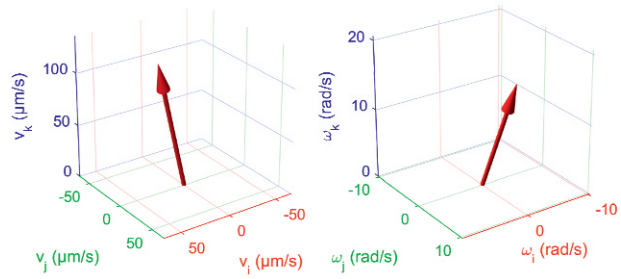
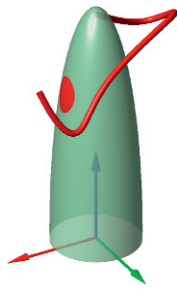
Movie S3. Flagellar shape reconstruction. We exploit the slow (incremental) rotational motion of the *Euglena* around the axis of its helical trajectory. As the *Euglena* rotates, at instants one beating period T_b apart, different views of the same flagellar configuration are exposed. This permits an algorithmic stereo matching reconstruction of the intrabeat flagellar shapes.

[Movie S3](#)



Movie S4. Variability of the flagellar beat among different observations. The reconstructed 3D flagellar shape of Cell1a* (green), conveniently scaled in both space and time, is superimposed (blue) on image data from the other five datasets. The good overlap suggests the existence of a distinctive *Euglena* beat style.

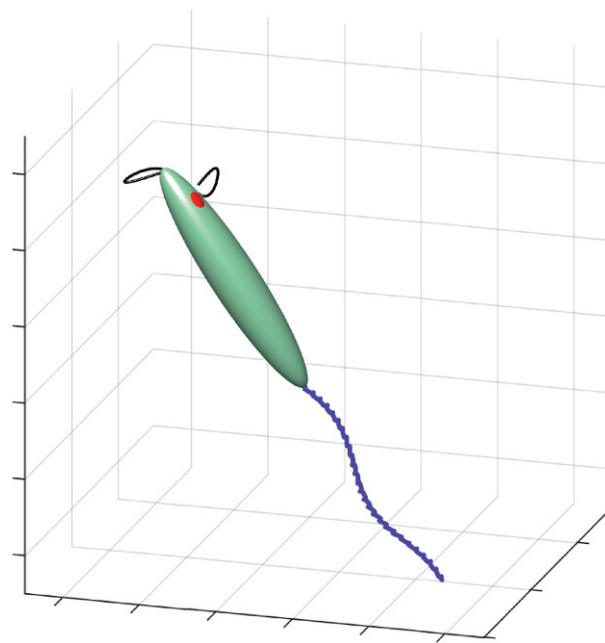
[Movie S4](#)



Movie S5. Comparison between flagellar shapes, during one beat, and the resulting translational and angular velocities (represented in the cell body reference frame coordinates).

[Movie S5](#)

$t = 1.200 \text{ s}$



Movie S6. Video summary. Reconstruction of the 3D kinematics of euglenoid flagellar swimming, starting from high-resolution 2D image recordings.

[Movie S6](#)